Emergence and stability of Majorana fermions in proximity-coupled topological insulator nanowires

by

Ashley M. Cook

B.Sc., The University of British Columbia, 2010

A THESIS SUBMITTED IN PARTIAL FULFILLMENT OF
THE REQUIREMENTS FOR THE DEGREE OF

MASTER OF SCIENCE

in

The Faculty of Graduate Studies

(Physics)

THE UNIVERSITY OF BRITISH COLUMBIA

(Vancouver)

July 2012

Abstract

A finite-length topological insulator nanowire, proximity-coupled to an ordinary bulk s-wave superconductor and subject to a longitudinal applied magnetic field is shown to realize a one-dimensional topological superconductor with an unpaired Majorana fermion localized at each end of the nanowire. Here we also show that the unpaired Majorana fermions persist in this system for any value of the chemical potential inside the bulk band gap of order 300 meV in Bi_2Se_3 by computing the Majorana number. From this calculation, we also show that the unpaired Majorana fermions persist when the magnetic flux through the nanowire cross-section deviates significantly from half flux quantum. Lastly, we demonstrate that the unpaired Majorana fermions persist in strongly disordered wires with fluctuations in the on-site potential ranging in magnitude up to the size of the bulk band gap. These results suggest this solid-state system should exhibit unpaired Majorana fermions under accessible conditions likely important for experimental study or future applications.

Preface

Chapter 3 is based on work conducted at UBC by Professor Marcel Franz and Ashley Cook. I was responsible for generating all numerical data and performing some of the analytical calculations.

A manuscript based on chapters 1 and 3 has been submitted for publication. I wrote most of the manuscript. This manuscript also includes an additional section II. C., "Majorana state in a finite-wire configuration" and associated appendix written by Mohammad Vazifeh not included in this thesis.

Chapter 3 also references small portions of a previously published paper[87] by Professor Franz and Ashley Cook, specifically those portions of the text referring to Figures 3.3, 3.4, 3.7, and 3.8, which were originally published in that paper. I collected all numerical data for this paper.

Table of Contents

List of Figures

Acknowledgements

The author gratefully acknowledges the guidance of Prof. Marcel Franz, who supervised this Masters thesis work and was an exceptional mentor. As well, many thanks to Conan Weeks, Prof. Ion Garate, Gilad Rosenberg, and Mohammad Vazifeh for countless helpful discussions.

Dedication

I dedicate this work to my parents and to the many friends I made during this degree who made it so much fun and who helped me to succeed.

Chapter 1

Introduction

1.1 Topological quantum computation

Considerable effort is being made around the world to build a practical quantum computer, since these devices are predicted to dramatically improve computational power for certain tasks [1]. Significant challenges remain, however. One of the most serious faced by many proposals is deterioration of stored information, due to quantum decoherence, too rapid for most applications [2]. Related schemes using topological quantum computers are predicted to avoid this difficulty, making them worthy of investigation [3].

In particular, solid state realizations of fermions that are their own antiparticles, called Majorana fermions, have been under intense theoretical study as a possible platform for this type of fault-tolerant quantum computation [4, 5].

1.2 Majorana fermions

1.2.1 Background

In 1937, Ettore Majorana first showed that the complex Dirac equation can be separated into a pair of real wave equations, each of which is satisfied by real fermionic fields [6]. Such a real fermionic field, denoted by Ψ, satisfies the property that $\Psi = \Psi^{\dagger}$. A particle created by this field, known as a Majorana fermion (MF), is therefore distinguished by the fact that it is its own antiparticle [7]. Having many properties which make them interesting from the standpoint of fundamental science, while also being a possible platform for fault-tolerant, scalable quantum computation[4, 5, 8–11], Majorana fermions are of tremendous interest to the condensed matter community. After intense effort, some proposals to realize Majorana fermions made in recent years seem to be bearing fruit, with signatures potentially of Majorana fermions already being reported[12–14]. Of the many devices proposed for harbouring Majorana fermions [7, 15], however, virtually all face considerable experimental challenges in achieving the conditions necessary for

Majorana fermion emergence. Additional hurdles are associated with the control and manipulation of MFs which is necessary for harnessing their potential for quantum computation. Thus, even if Majorana fermions have indeed been conclusively observed, there remains a need for more accessible platforms with which to realize MFs sufficiently robust for applications.

1.2.2 Applications in topological quantum computation

A system of N spatially-separated Majorana fermions is predicted to satisfy non-Abelian statistics, implying that such a system has an N-quasiparticle ground state that is degenerate. This degeneracy allows adiabatic interchange of the quasiparticles, or braiding, to correspond to unitary operations on the ground state. For Majorana fermions, it has also been shown that the only way to perform unitary operations on the ground state - which could be used for computing - is by braiding, and these operations are dependent only on the topology of the braid. Since the system is in a topological phase when Majorana fermions are present, this degenerate ground state is also separated from the rest of the spectrum by an energy gap known as the mini-gap. If the temperature is much lower than the mini-gap, and the system is weakly perturbed using frequencies much smaller than the gap, the system evolves only within the ground state subspace [16].

All of these features combined mean that a system of spatially-separated Majorana fermions could be used as a quantum computer that is immune to the tremendous obstacle faced by most other proposed platforms for quantum computing known as decoherence [17]. Experimental confirmation of the existence of Majorana fermions is a crucial first step towards practical quantum computing, but it is imperative that platforms possessing robust Majorana fermions under stable conditions be identified and developed.

1.2.3 Existing theoretical proposals for realizing Majorana fermions

There is no shortage of proposals for realizing Majorana fermions experimentally. Earlier suggestions for physical systems that support Majorana fermion states include fractional quantum Hall states at filling $\nu = \frac{5}{2}$[18] and Helium-3[19]. These ground-breaking proposals are thought to be extremely challenging to realize experimentally[20], however. We will discuss the many other proposals and comment on the experimental challenges they face below.

2D topological insulators have long been proposed as platforms for realizing Majorana zero-modes, for instance, having the advantages of greatly facilitating Josephson-based Majorana detection, long considered to be smoking gun confirmation of the presence of Majorana zero-modes[15], as well as being unaffected by non-magnetic disorder due to time-reversal invariance[21, 22] and, in principle, possessing a large pairing gap exhibited by the parent superconductor[21, 23]. However, of many materials predicted to be 2D topological insulators[24–30], only one, HgTe, has been confirmed experimentally thus far[31, 32], although there has also been some evidence recently that InAs/GaSb quantum wells may also exhibit a topological insulator phase[33, 34]. 2D semiconductor heterostructures have also shown promise as platforms for realizing Majorana zero-modes, but face challenges due to small spin-orbit energies[35, 36], a need for difficult-to-engineer, high-quality interfaces, and limited tunability[15].

An innovative proposal for realizing Majorana zero-modes in three dimensional topological insulators due to Fu and Kane exists[37], but this proposal, while ground-breaking, faces considerable challenges given that time-reversal symmetry must be broken to achieve Majorana zero-modes, making the device vulnerable to non-magnetic disorder[15]. There have also been many proposals based on Su_2RuO_4, but even in the simplest of these proposals, the mini-gap protecting Majorana zero-modes from excited states is in the milliKelvin range[15], and a beautiful proposal for realizing Kitaev's 1D toy model along an ordinary $\frac{hc}{2e}$ vortex line threading a layered spinful $p+ip$ superconductor likely to be Su_2RuO_4 currently faces the same problem[15, 38].

There is great interest in realizing Majorana zero-modes in one dimensional systems, because they have generally been predicted to remain separated from excited states by a larger energy gap than in other proposals[15]. Conventional 1D wires with sizeable spin-orbit coupling, proximate to s-wave superconductors, and subject to modest magnetic fields[20, 39] are seen as very promising platforms for first experimental realization of Majorana zero-modes[15]. These proposals must overcome numerous issues, however, such as positioning of the chemical potential in a rather small interval of roughly 1 K over distances long compared to the wire's coherence length[15]. This constraint could be relaxed by applying larger magnetic fields, but this introduces other difficulties[15]. Tuning of the chemical potential could likely be even more difficult due to disorder-induced fluctuations in the chemical potential, since the topological phase corresponding to the presence of Majorana zero-modes appears only at finite magnetic fields in these devices, so Anderson's theorem does not protect the gap against non-magnetic disorder,

which is always pair-breaking according to many previous studies[21, 40–47]. Further, since the ratio of Zeeman energy to spin-orbit energy is small for both wires made of InAs and InSb[48], disorder is likely to play a non-trivial role[15]. Although there have been efforts to ameliorate this issue by eliminating an applied magnetic field[49, 50] from the device or reducing it[51, 52], these approaches can also lead to complications that can potentially cause the Majorana zero-modes to disappear[49, 51].

The above conventional 1D wire proposals further face the challenge that multiple sub-bands are usually occupied in these wires and gating into the lowest sub-band regime is potentially non-trivial, especially if these wires are in close proximity to a superconductor as proposed[15]. Multichannel wires have been shown to support the 1D topological superconductor state leading to Majorana zero-modes away from the lowest sub-band limit[43, 46, 53, 54], but these systems still require some degree of gating, leading to proposals of increasing complexity involving regular arrays of superconducting islands in contact with the wire[55–57]. Such work has even led to the ingenious proposal of a chain of quantum dots that would be bridged by superconducting islands[57], but reaching the regime where only a comparatively small number of quantum dots would be needed would require very fine-tuning that would likely suffer from strong randomness[15]. Carbon nanotubes, also suggested as hosts for Majorana zero-modes, face considerable challenges in reaching the spinless regime with proximity-induced pairing required[58–60], while proposals involving half-metallic ferromagnetic wire also face challenges, such as the need to couple to non-centrosymmetric superconductors with spin-orbit coupling[61, 62].

Despite these tremendous challenges, there have been promising experimental results for Majorana fermions based on some of these proposals. Josephson effects at the surface of a variety of 3D topological insulators with superconducting electrodes have been observed [12, 63–68]. While these experiments, and related Andreev conductance measurements[69–72] show interesting and unusual features, these cannot be readily attributed to the single Majorana zero-mode (typically only one out of 10^5 modes)[15].

1.2.4 Experimental progress

The nanowire-based proposal of Lutchyn et al. [39] and Oreg et al. [20] has also led to convincing evidence for a Majorana zero-mode in an InSb nanowire as reported by Kouwenhoven and his group [13]. If indeed Majorana zero-modes have finally be observed, however, there still remains a need for devices in which MFs can be realized under more accessible condi-

tions, are robust, and can finally be manipulated for topologically-protected computation, motivating the results we present here on a proposal in which Majorana fermions occur under a wide-range of accessible conditions robustly.

Chapter 2

Setup

2.1 Topological insulators

In an insulator, such as solid argon, an energy gap separates occupied valence band states from empty conduction band states. The same is true for a semiconductor, although the energy gap is smaller. These two states are, in fact, topologically equivalent, in the sense that one could imagine tuning parameters of the Hamiltonian describing the insulator continuously in order to produce the Hamiltonian of the semiconductor without closing this energy gap. If we generalize, and consider states with different numbers of trivial core bands to be equivalent, then the insulator and semiconductor are further equivalent to the vacuum in the same sense, which also has an energy gap for pair production, a conduction band, and a valence band according to Dirac's relativistic theory[73].

The *topological* insulator also possesses an energy gap in the bulk, but is, in fact, a phase of matter topologically-distinct from the vacuum, meaning that the Hamiltonian describing the topological insulator cannot be deformed into the Hamiltonian for the vacuum state by continuous tuning of its parameters without closing the bulk band gap[73]. As explained more generally below, closure of the bulk band gap at the boundary between this topological insulator phase and a phase equivalent to the vacuum, which is necessary to transition from the former phase to the latter, leads to an unusual property of topological insulators: While they are insulating in the bulk, they possess unusual metallic states on their surfaces. These surface states, it turns out, can be used under certain conditions to construct Majorana fermions.

2.2 Topological phases and invariants

Depending on the dimension as well as the presence or absence of time reversal symmetry and/or particle-hole symmetry in a given class of Hamiltonians, in fact, different numbers of topologically distinct phases of matter can

be characterized[73]. There are ten unique classes in all, describing all states of matter possessing energy gaps (all insulators and also superconductors)[74–77]. Topological invariants count and distinguish these topologically-distinct states for each Hamiltonian class. A one-dimensional or two-dimensional topological insulator, for instance, is characterized by a single $\mathbb{Z}_2$ topological invariant, meaning that it is characterized by a Hamiltonian which can, through tuning of its parameters, describe just two topologically-distinct states of matter. A three-dimensional topological insulator, however, is characterized by four $\mathbb{Z}_2$ topological invariants $(\nu_0; \nu_1\nu_2\nu_3)$, meaning that it is described by a Hamiltonian that can be tuned to achieve sixteen topologically-distinct phases of matter[78–80]. Although this thesis describes a device that uses a nanowire made of a 3D topological insulator, we will subsequently show, in Chapter 3, that the nanowire can be treated theoretically largely as a one-dimensional system described by a $\mathbb{Z}_2$ topological invariant known also as the Majorana number[81], which is discussed in further detail as necessary in Chapter 3.

Topological classification of gapped band structures leads to a feature of topological phases very relevant to this Masters work: The existence of gapless conducting states at interfaces where the topological invariant changes. Such edge states are observed at the interface between the integer quantum Hall state and vacuum[82], and can be understood in terms of the skipping motion electrons execute as their cyclotron orbits bounce off the edge. These edge states arise from the requirement that, in order to transition between two topologically-distinct phases of matter, one must close the bulk band gap of the system. Otherwise, it is impossible for the topological invariant to change. Low energy electronic states therefore occur in the region where the energy gap passes through zero[73].

2.3 Motivation for using topological insulators to realize Majorana fermions

An operator Ψ satisfying $\Psi = \Psi^\dagger$ in a condensed matter setting can be constructed as a linear combination of an electron creation operator and annihilation operator such as $\Psi = (c_\uparrow + c_\uparrow^\dagger)/\sqrt{2}$. (Thus, a Majorana fermion, in condensed matter systems, can be thought of as a linear combination of an electron and a hole.) Superconductivity, as well as other phenomena which induce pairing and condensation of fermions, therefore seem well-suited to the task of constructing Majorana fermions. In almost all cases, however, superconductivity results from *s*-wave pairing of electrons and holes carry-

ing *opposite* spins. Quasiparticle operators then (schematically) take the form $\Phi = uc_{\uparrow}^{\dagger} + \nu c_{\downarrow}$, for which $\Phi \neq \Phi^{\dagger}$. One way to overcome this issue and construct quasiparticles created by operators such as Ψ is to induce superconductivity in a *spinless* metal. By Pauli exclusion, Cooper pairing in such a system must occur with odd parity, which results in p-wave superconductivity in one dimension. This kind of superconductor realizes a topological phase that, most relevant to this thesis, supports Majorana zero-energy modes localized at the boundaries between the 1D topological p-wave superconducting phase and the vacuum[15].

Localized zero-energy Majorana end-states are expected to appear at the ends of the nanowire in part because the TI nanowire, modeled as a 1D topological insulator, is in a topological phase while the vacuum bordering the nanowire is a non-topological, or trivial, phase of matter[15]. Since these phases cannot be smoothly connected, the energy gap must close at each end of the nanowire, allowing for zero-modes to exist in these locations. Majorana zero-modes in particular are expected at the ends of the nanowire as a result of a key property of the dispersion of the infinitely-long 1D TI nanowire under the operating conditions of our device, which are outlined in Chapter 3. In both the topological and trivial phases, Kramer's theorem requires that bands of a dispersion be at least two-fold degenerate for time-reversal invariant momenta such as $k = 0$ and $k = \pi/a$, where a is the lattice spacing. Away from these points, a spin-orbit interaction will split the degeneracy. There are two ways in which the states at $k = 0$ and $k = \pi/a$ can connect: They can connect pairwise, such that an even number of bands intersects the chemical potential in the right half of the Brillouin zone, or an odd number of bands can intersect the chemical potential in the right half of the Brillouin zone[73]. The latter situation occurs under operating conditions for our device and corresponds, in one dimension, to topologically-protected end-states, and to the topological phase. Intersection of the chemical potential by an odd number of bands in the right half of the Brillouin zone also makes the topological phase a spinless metal with the potential for generating Majorana fermions once it becomes superconducting[15].

With this motivation, we can begin to discuss the proposal for realizing unpaired Majorana fermions based on proximity-coupled topological insulator nanowires in Chapter 3.

Chapter 3

Proposal For Realizing Unpaired Majorana Fermions Based On Proximity-Coupled Topological Insulator Nanowires

3.1 Introduction

The focus of this Masters work is a proposal for a new type of solid-state device that can serve as a host for unpaired Majorana fermions under a wide range of experimentally accessible conditions. Depicted schematically in Fig. 3.1, the device consists of a nanowire (wire with nanometer-scale cross-section) made of a strong topological insulator (STI), such as Bi_2Se_3 or Bi_2Te_2Se, placed on top of an ordinary s-wave superconductor (SC), with an applied magnetic field along the axis of the nanowire. When the magnetic flux through the nanowire cross-section is close to a half-integer multiple of the fundamental flux quantum $\Phi_0 = hc/e$, the topologically protected surface state realizes a one-dimensional *topological superconductor* [81] with Majorana fermions localized near the ends of the wire. We show that MFs are remarkably stable in this device, making it unique amongst the many proposals for observing MFs in solid-state systems and a significant advancement towards study of MFs and development of MF-based technology.

We note that Bi_2Se_3 nanowires and nanoribbons have been synthesized and can exhibit diverse morphologies controllable by growth conditions[83]. Aharonov-Bohm (AB) oscillations in the longitudinal magneto-resistance of Bi_2Se_3 nanoribbons have also been observed, proving the existence of a coherent surface conducting channel[84]. Studies of magneto-resistance of Bi_2Se_3 nanoribbons under a variety of magnetic field orientations also reveal a linear magneto-resistance that persists to room temperature and is

consistent with transport through topological surface states[85]. Lastly, the superconducting proximity effect and possible evidence for Pearl vortices has been observed in Bi_2Se_3 nanoribbons[86]. This experimental progress suggests our proposed device may be realized experimentally with relative ease.

Stability is confirmed by showing that the degenerate quasiparticle ground state is separated from excited states by an energy gap close to the superconducting (SC) gap which can be as large as ~ 10 meV, through study of a low-energy analytical theory and numerical study of an explicit lattice-model Hamiltonian. We also compute the topological phase diagram for the system numerically to show that MFs exist in the system for any value of the chemical potential in the bulk band gap of the TI (for Bi_2Se_3, ~ 300 meV). Furthermore, we find that the topological phase corresponding to the presence of MFs persists even when the chemical potential is in the bulk conduction band, although, since we observe rapid collapse of the excitation gap in this regime, this result is of limited experimental relevance.

These results also support additional explicit numerical studies of the robustness of MFs against non-magnetic disorder also discussed, which show that the MFs persist in the presence of fluctuations in the on-site chemical potential in an explicit lattice model Hamiltonian on the order of the bulk band gap (300 meV). As such, previous expectations that MFs would be robust against non-magnetic disorder according to Anderson's theorem, because time reversal symmetry (TRS) holds in this device under operating conditions [87], are here confirmed.

In the most promising of other proposals, the MFs are protected by an SC gap of at most 1 meV, and the chemical potential must also be tuned to lie within a window of the same size[20, 39]. Although these requirements are possible to achieve in experiments on individual wires [13], such fine tuning will be difficult to replicate in more complex setups, i.e. those containing wire networks necessary for MF manipulation[91]. Furthermore, other proposals are not predicted to possess MFs under TR-invariant conditions, meaning these devices are not expected to be robust against non-magnetic disorder. Therefore MFs constructed in these proposals might be too delicate to be useful in practical applications. Our results on the remarkable stability of MFs in the TI nanowire-based proposal therefore outline a practical route towards applications based on the physics of Majorana fermions.

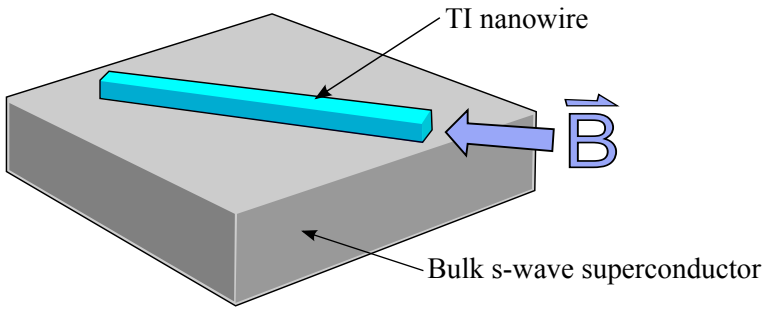

Figure 3.1: Schematic of the proposed device.

3.2 Low-energy theory of a TI nanowire with magnetic and superconducting order

We begin by presenting the low-energy analytical theory of the device [87] in greater detail to facilitate later discussion of the novel results on stability, as this foundation is later used to understand the new results.

First, we motivate the proposal with study of a cylindrical TI nanowire proximity-coupled to a bulk s-wave SC as the greater symmetry of this system permits analytical study of the low-energy fermionic excitations on the surface of the nanowire.

The low-energy fermionic excitations on the surface of the topological insulator are governed by the Dirac Hamiltonian [92]

$$h_0 = \frac{v}{2}\big[\hbar\nabla\cdot\hat{\mathbf{n}} + \hat{\mathbf{n}}\cdot(\mathbf{p}\times\mathbf{s}) + (\mathbf{p}\times\mathbf{s})\cdot\hat{\mathbf{n}}\big], \tag{3.1}$$

where $\hat{\mathbf{n}}$ is a unit vector normal to the surface, $\mathbf{p} = -i\nabla$ is the momentum operator and $\mathbf{s}$ is the vector of Pauli matrices in the spin space. We will also include the effect of a magnetic coating on the TI nanowire by adding an additional term, $h_m = \mathbf{s}\cdot\mathbf{m}$, to the Hamiltonian. Later, we will show that this term is not necessary for Majorana zero-modes to emerge in the device, but its inclusion will be convenient in calculations.

Let us now consider the specific case of a cylindrical topological insulator nanowire of radius R with magnetic field $\mathbf{B}$ applied along the $\hat{z}$-axis as shown in Fig. 3.2. The unit vector $\hat{\mathbf{n}}$ is then taken to be normal to the curved surface of the nanowire. To include a flux Φ through the end of the wire (in the $\hat{z}$ direction) as proposed, we replace the momentum operator $\mathbf{p}$ in Eq. (3.1) with $\boldsymbol{\pi} = \mathbf{p} - (e/c)\mathbf{A}$, where $\mathbf{A} = \eta\Phi_0(\hat{z}\times\mathbf{r})/2\pi r^2$ is the vector

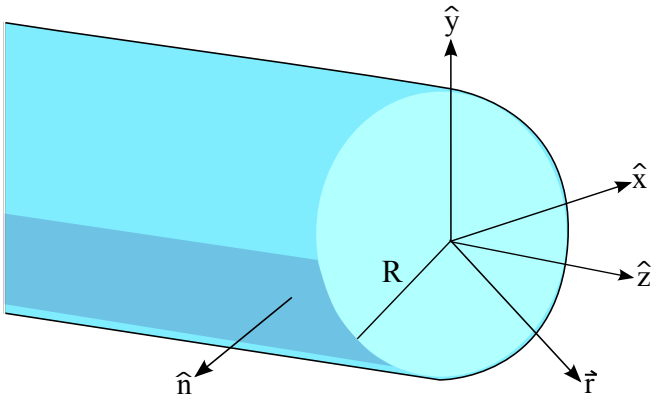

Figure 3.2: Schematic of the device simplified for analytical study, in which a cylindrical TI nanowire is substituted for a more realistic TI nanowire with square cross-section. Magnetic field **B** is still applied along the axis of the wire taken to coincide with the z-direction.

potential and Φ_0 is the flux quantum. Therefore, suppressing $v\hbar$, we now have the Hamiltonian,

$$h = \frac{1}{2r}\mathbb{I} + (\hat{\mathbf{n}} \times \boldsymbol{\pi}) \cdot \mathbf{s} + \mathbf{s} \cdot \mathbf{m}. \tag{3.2}$$

Taking $\mathbf{m} = m\hat{z}$, we can rewrite the Hamiltonian in cylindrical coordinates as

$$h = \frac{1}{2R}\mathbb{I} + s_1 k \sin(\phi) - s_2 k \cos(\phi) - s_3 \left(\frac{i}{R}\partial_\phi + \frac{\eta}{R} \right) + m s_3. \tag{3.3}$$

To diagonalize this Hamiltonian for an infinitely long wire, we exploit the translational and rotational symmetries and write a solution ψ_{kl} of the form

$$\psi_{kl}(z, \varphi) = e^{i\varphi l} e^{-ikz} \begin{pmatrix} f_{kl} \\ e^{i\varphi} g_{kl} \end{pmatrix} \tag{3.4}$$

With this ansatz, our Hamiltonian is

$$\tilde{h}_{kl} = s_2 k + s_3 [(l + \frac{1}{2} - \eta)/R + m]. \tag{3.5}$$

The spectrum E_{kl} for $m = 0$, if $v\hbar$ is reinstated, is then

$$E_{kl} = \pm v\hbar \sqrt{k^2 + \frac{(l + \frac{1}{2} - \eta)^2}{R^2}}. \tag{3.6}$$

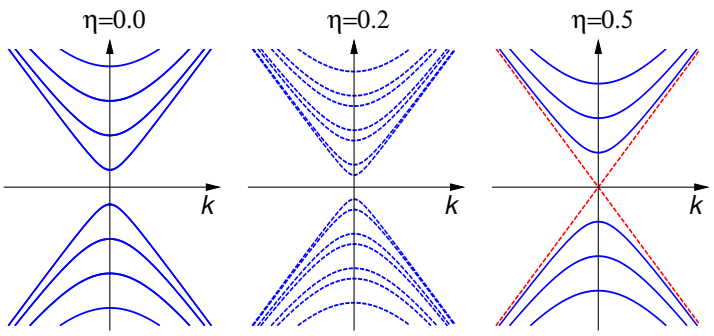

Figure 3.3: Surface state excitation spectra E_{kl} for various values of magnetic flux $\Phi = \eta\Phi_0$. Solid and dashed lines indicate doubly degenerate and non-degenerate bands, respectively.

Here k labels momentum eigenstates along the cylinder while $l = 0, \pm 1, \ldots$ is the angular momentum. We see that the spectrum has a gapless branch for $\eta = n + \frac{1}{2}$, where n is any integer ($\eta = \Phi/\Phi_0$ measures the magnetic flux through the wire cross section in the units of flux quantum $\Phi_0 = hc/e$). The periodicity $\eta \to \eta + n$ with n integer in Eq. (3.6) reflects the expected Φ_0-periodicity in the total flux. We now notice that, for $\eta = 0$, all branches of E_{kl} are doubly degenerate (Fig.3.3). For $\eta \neq 0$, however, the degeneracy is lifted and one can always find a value of the chemical potential μ that intersects the bands of the dispersion in the right half of the Brillouin zone (each such intersection is known as Fermi point) an odd number of times.

One can formalize the above argument by considering Kitaev's Majorana number $\mathcal{M}$, defined as $\mathcal{M} = (-1)^{\nu}$, where ν represents the number of Fermi points, or points of intersection between the chemical potential and bands of the dispersion, for $k > 0$[81]. In the limit of weak pairing, $\mathcal{M} = -1$ indicates the existence of unpaired Majorana fermions at the ends of the wire. Fig. 3.4 shows $\mathcal{M}$ calculated from the spectrum as a function of μ and η. We observe, specifically, that when $\eta = 1/2$, i.e., for the flux equal to a half-integer multiple of Φ_0, Majorana fermions will appear for any value of the chemical potential (as long as it lies inside the bulk gap). This result is easily understood by noting that for $\eta = 1/2$ the gapless $l = 0$ branch is non-degenerate while the remaining branches are all doubly degenerate. Thus, the number of Fermi points for $k > 0$ is odd for any value of μ. Pairing induced by the proximity effect in such a state is then expected to drive the system into a topological phase. Thus, while the semiconductor

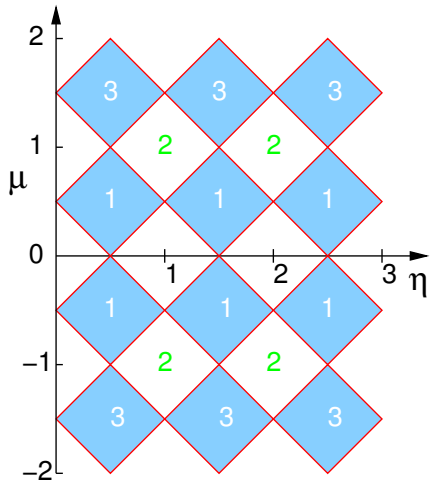

Figure 3.4: Kitaev's Majorana number: $\mathcal{M} = -1(+1)$ in shaded (white) regions. Numerals inside the squares indicate the number of Fermi points for $k > 0$.

wire proposal [20, 39] only possesses Majorana fermions for values of the chemical potential in a ~ 1 meV interval, our proposal possesses Majorana fermions for any value of the chemical potential μ inside the 300 meV bulk band gap of Bi_2Se_3. Fine-tuning of the chemical potential is unnecessary in our device at $\eta = 1/2$ due to the specific pattern of degeneracies of the bands which is in turn protected by the Kramers theorem.

To study the emergence of Majorana fermions in the simplest possible setting, we now focus on the $\eta = \frac{1}{2}$ case and consider values of the chemical potential satisfying $|\mu| < \frac{v\hbar}{R}$, i.e. intersecting only the $l = 0$ branch of the spectrum. The Hamiltonian for this branch then becomes $h_k = ks_2 - \mu + ms_3$, where we have explicitly included the chemical potential term. The Bogoliubov-de Gennes Hamiltonian describing the proximity-induced superconducting order in the nanowire can be written, in the second-quantized notation, as $H = \sum_k \Psi_k^\dagger \mathcal{H}_k \Psi_k$ with $\Psi_k = (f_k, g_k, f_{-k}^\dagger, g_{-k}^\dagger)^T$ and

$$\mathcal{H}_k = \begin{pmatrix} h_k & \Delta_k \\ -\Delta_{-k}^* & -h_{-k}^* \end{pmatrix}. \tag{3.7}$$

For the surface state, $\eta = 1/2$ represents a $\mathcal{T}$-invariant point at which $h_{-k}^* =$

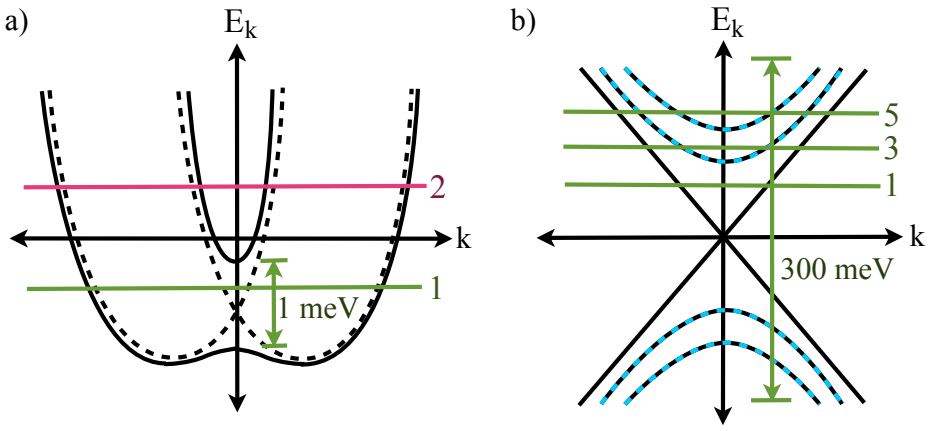

Figure 3.5: The normal state dispersion under conditions required for emergence of Majorana fermions for (a) the Rashba-coupled semiconductor quantum wire proposal in [20, 39], where the dispersion is shown without Zeeman coupling (dashed lines) and with Zeeman coupling, and (b) our topological insulator nanowire proposal, with doubly-degenerate bands shown as black and blue dashed lines. Green and pink horizontal lines represent the level of the chemical potential and a number to the right of a line indicates the number of Fermi points in the right half of the Brillouin zone at that value of the chemical potential. Vertical green lines indicate the interval inside which the chemical potential can be tuned to yield Majorana fermions in the corresponding SC state.

h_k. Therefore, $\mathcal{H}_k$ can be written as

$$\mathcal{H}_k = \begin{pmatrix} h_k & \Delta_k \\ -\Delta_{-k}^* & -h_k \end{pmatrix}. \tag{3.8}$$

In the following, we consider the simplest s-wave pairing potential $\Delta_k = \Delta_0 i\mathbf{s}_2$, with Δ_0 a (complex) constant order parameter, which corresponds to the pairing term $\Delta_0(f_k^\dagger g_{-k}^\dagger - g_k^\dagger f_{-k}^\dagger)$. It is useful to note that this form of Δ_k actually implies a vortex in the SC order parameter, as can be seen by transforming $\mathcal{H}_k$ back into the original electron basis, i.e. undoing the transformation indicated in Eq. (3.4). The phase of the order parameter in this basis winds by 2π on going around the cylinder as required in the presence of the applied magnetic field whose total flux is $\Phi_0/2$.

Introducing Pauli matrices τ_α in the Nambu space and assuming Δ_0 real,

we can write

$$\mathcal{H}_k = \tau_3(ks_2 - \mu) + \tau_3 s_3 m - \tau_2 s_2 \Delta_0. \tag{3.9}$$

(Here we have again taken $v = \hbar = 1$.) The spectrum for this Hamiltonian is $E_k = \pm(k^2 + \mu^2 + m^2 + \Delta_0^2 \pm 2(k^2\mu^2 + \mu^2 m^2 + m^2\Delta_0^2)^{1/2})^{1/2}$. We now consider a special case when $\mu = 0$. The Hamiltonian simplifies, $\mathcal{H}_k = \tau_3 s_2 k + \tau_3 s_3 m - \tau_2 s_2 \Delta_0$ and the spectrum assumes a simple and suggestive form

$$E_k = \pm\sqrt{k^2 + (m \pm \Delta_0)^2}. \tag{3.10}$$

We observe that the spectrum is fully gapped in the presence of either SC or magnetic order but has a gapless branch when $m = \pm\Delta_0$. Thus, we expect a topological phase transition at this point. Consequently, we expect gapless modes to exist at an interface between SC and magnetic domains in a wire.

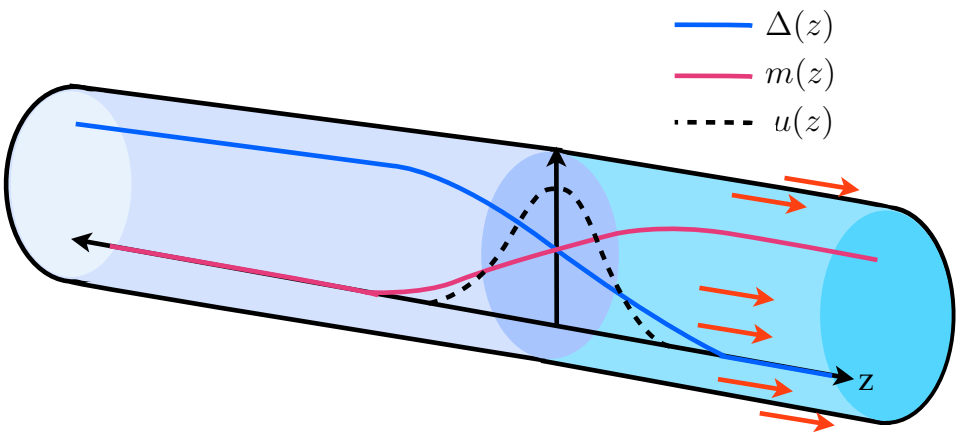

Figure 3.6: A convenient possible choice for the SC/magnetic domain wall at $z = 0$. $\Delta(z)$ is the SC order parameter and $m(z)$ the magnetic order parameter. A dashed line shows the zero-mode solution $u(z)$ for this domain wall. This particular choice of boundary conditions can be used to show Majorana fermions occur at the ends of the TI nanowire irrespective of precise boundary conditions.

Now consider spatially varying $m(z)$ and $\Delta(z)$ such that $m(0) = \Delta(0)$ as sketched in Fig. 3.6. With these choices for the order parameters, we expect the spectrum to be gapped far away from the domain wall, but we expect gapless modes localized near $z = 0$. To determine if there are any fermionic

zero modes, we rotate $\mathcal{H}_k$ in $s-\tau$ space so that the rotated Hamiltonian is completely off-diagonal. That is, we work with $\tilde{\mathcal{H}}_k = U\mathcal{H}_k U^{-1}$, where

$$U = e^{-i\frac{\pi}{4}s_2}e^{-i\frac{\pi}{4}\tau_2}. \tag{3.11}$$

Then $\tilde{\mathcal{H}}_k = \tau_1 s_2 k + \tau_1 s_1 m - \tau_2 s_2 \Delta$, so $\tilde{\mathcal{H}}_k$ is of the form

$$\tilde{\mathcal{H}}_k = \begin{pmatrix} 0 & D_k \\ D_k^\dagger & 0 \end{pmatrix}, \tag{3.12}$$

where $D_k = s_2 k + s_1 m + i s_2 \Delta$.

We now replace $k \to -i\partial_z$ and look for solutions $\tilde{\Psi}(z)$ satisfying

$$\tilde{\mathcal{H}}_k \tilde{\Psi}(z) = 0. \tag{3.13}$$

Taking $\tilde{\Psi}(z) = (\psi_1, \psi_2, \psi_3, \psi_4)^T$ and reinstating v, Eq. (3.13) yields four independent equations:

$$(+v\partial_z + m + \Delta)\psi_1 = 0 \tag{3.14}$$
$$(-v\partial_z + m - \Delta)\psi_2 = 0 \tag{3.15}$$
$$(+v\partial_z + m - \Delta)\psi_3 = 0 \tag{3.16}$$
$$(-v\partial_z + m + \Delta)\psi_4 = 0 \tag{3.17}$$

Here we have suppressed the z dependence. The solution $u(z)$ of an equation of the form

$$[v\partial_z + \omega(z)]\, u_z = 0, \tag{3.18}$$

a Jackiw-Rossi zero mode [93], can be written as

$$u(z) = u_0 e^{\frac{-1}{v}\int_0^z dz'\omega(z')}. \tag{3.19}$$

This solution is normalizable provided that $\omega(z)$ has a soliton profile, i.e. is proportional to $\mathrm{sgn}(z)$ for large $|z|$. According to our assumptions, $m(z) + \Delta(z) > 0$ for all values of z, so there is no normalizable solution for ψ_1 or ψ_4. With $v > 0$, there is also no normalizable solution for ψ_2, but there is one for ψ_3:

$$\psi_3(z) = u_0 e^{\frac{-1}{v}\int_0^z dz'(m(z')-\Delta(z'))}. \tag{3.20}$$

(For $v < 0$, ψ_2 would be the normalizable solution instead.) Thus, for $\Delta(z)$, $m(z)$ as given in Fig. 3.6, our Hamiltonian has a single zero-mode solution of the form $\tilde{\Psi}_0 = (0,0,1,0)^T u(z)$ localized near the domain wall at $z = 0$. This solution is valid as long as $v > 0$ and $m(z) - \Delta(z) \to \pm\text{const}$ for $z \to \pm\infty$. To

see if the zero mode $\tilde{\Psi}_0(z)$ corresponds to a Majorana fermion, we undo the unitary rotation and inspect the corresponding solution $\Psi_0(z) = U^{-1}\tilde{\Psi}_0(z)$, which is

$$\Psi_0(z) = \frac{1}{2}(1,-1,1,-1)^T u(z). \tag{3.21}$$

In second quantization, the field operator destroying the particle in the state $\Psi_0(z)$ is

$$\hat{\psi}_0 = \frac{1}{2}\int dz u(z)\left[f(z) - g(z) + f^\dagger(z) - g^\dagger(z)\right]. \tag{3.22}$$

where $f(z)$, $g(z)$ are real-space versions of the f_k, g_k operators in Ψ_k . Since $u(z)$ is real, it holds that $\hat{\psi}_0^\dagger = \hat{\psi}_0$, so Ψ_0 represents a Majorana fermion.

With a few additional observations, the above calculation can be used to show that an additional unpaired Majorana mode exists at the SC end of the wire irrespective of boundary conditions. First, recall that in a finite system Majoranas always come in pairs, since they are formed from ordinary fermions [15]. This second Majorana fermion, being a zero-mode, cannot not exist in the nanowire bulk where the spectrum is gapped. It cannot exist at the magnetic end because the magnetic order does not support the requisite particle-hole mixing. The second MF must therefore be at the SC end of the nanowire, irrespective of the exact boundary condition. From this, we can argue that the special conditions used to establish the existence of unpaired MFs in the device are unnecessary: The zero-modes in fact exist in the device under generic boundary conditions as confirmed by explicit numerical study using a lattice model, discussed in section III. A specific example of Majorana end-states obtained in such a lattice calculation under general conditions is given in Sec. IV.A below.

3.2.1 Energy gap protecting Majorana zero-modes

As mentioned in [95], in order to detect and manipulate MFs under experimentally accessible conditions it is crucial that they are protected from all other excitations by a gap. The latter is often refered to as a 'minigap' because typically there will be other excitations inside the bulk gap. We study the minigap in this TI nanowire-based device both analytically and numerically.

In this section we estimate the minigap for the superconducting TI nanowire using the analytical low-energy theory. Specifically, we wish to find the lowest non-zero eigenvalue of $\tilde{\mathcal{H}}_k$ defined in Eq. (3.12). We start by squaring the Hamiltonian. We find, with $k \to -i\partial_z$ and $D_k^\dagger D_k \to D^\dagger D$,

$$D^\dagger D = \partial_z^2 + \partial_z\left[\Delta(z) - s_3 m(z)\right] + \left[\Delta(z) - s_3 m(z)\right]^2. \tag{3.23}$$

The two independent equations in $D^\dagger D$ can more conveniently be written as $(D^\dagger D)_+$ and $(D^\dagger D)_-$, where

$$\left(D^\dagger D\right)_\pm = \partial_z^2 + \partial_z \left[\Delta(z) \mp m(z)\right] + \left[\Delta(z) \mp m(z)\right]^2. \tag{3.24}$$

To find the energy of the first excited state, we look for solutions ψ satisfying

$$h\psi = \epsilon\psi, \tag{3.25}$$

where $h = \tilde{\mathcal{H}}^2$ and $\epsilon > 0$. We consider $m(z)$, $\Delta(z)$ such that $\Delta(z) + m(z)$ =const for each z, and $\Delta(z) - m(z) = f(z)$ having a soliton profile, e.g. we may take $f(z) = \Delta_0 \tanh(z/\xi)$, as shown in Fig. 3.6. Then $(D^\dagger D)_-$ yields no bound states. $(D^\dagger D)_+$, however, has the form, with velocity v restored,

$$(D^\dagger D)_+ = -v^2\partial_z^2 + v\partial_z f(z) + f^2(z) \tag{3.26}$$

For bound-state energies much less than Δ_0, $f(z)$ can be approximated as linear in the vicinity of $z = 0$. With $f(z) \simeq -\Delta_0 \frac{z}{\xi}$, where ξ is the length scale over which the SC order parameter varies near the domain wall, we then have

$$(D^\dagger D)_+ = -v^2\partial_z^2 - \frac{v\Delta_0}{\xi} + \left(\frac{\Delta_0}{\xi}\right)^2 z^2. \tag{3.27}$$

This is the Hamiltonian for the harmonic oscillator with the identification $\frac{\hbar^2}{2m} = v^2$, $\frac{m\omega^2}{2} = \left(\frac{\Delta_0}{\xi}\right)^2$, and $\hbar^2\omega^2 = 4v^2\frac{\Delta_0^2}{\xi^2}$. Therefore, allowed eigenenergies of $(D^\dagger D)_+$ bounded above by Δ_0^2 are

$$\epsilon_n = \hbar\omega(n + \frac{1}{2}) - \frac{v\Delta_0}{\xi} = \frac{2\hbar v\Delta_0}{\xi} n, \tag{3.28}$$

where n is any non-negative integer. The energy spectrum of $\tilde{\mathcal{H}}$ in this approximation is then

$$E_n = \pm\sqrt{\epsilon_n} = \pm\sqrt{\frac{2\hbar v\Delta_0}{\xi} n}. \tag{3.29}$$

Since ξ is the length scale over which the SC order parameter varies near the wire end, it is at most the SC coherence length $\frac{\hbar v}{\pi\Delta_0}$. The minimum energy of the first excited state E_1 is then

$$E_1 = \Delta_0\sqrt{2\pi}, \tag{3.30}$$

which is already greater than Δ_0. Therefore, there are no excited states where the linear approximation holds. There can be some at energies close to Δ_0 and this is consistent with numerical results presented in [87].

We also note that the calculation presented above is valid in the special case $\mu = 0$. For non-zero chemical potential the situation is more complicated and we are not able to find a simple analytic solution for the excited states in this case. Since the density of states of the underlying Dirac semimetal grows with increasing energy we expect there to be more low-lying excited states when $\mu \neq 0$ and thus reduced minigap. This expectation is indeed confirmed by our numerical simulations discussed below.

3.3 Results on stability of Majorana fermions

3.3.1 Lattice model

We establish the stability of Majorana fermions in the nanowire through a combination of additional analytical insights and numerical studies using the same concrete lattice model in [87] for the Bi_2Se_3 family of materials [94] given by Fu and Berg [96] regularized on a simple cubic lattice. This model is defined by a k-space Hamiltonian

$$h_{\mathbf{k}} = M_{\mathbf{k}}\sigma_1 + \lambda\sigma_3(s_2 \sin k_x - s_1 \sin k_y) + \lambda_z\sigma_2 \sin k_z, \tag{3.31}$$

with $M_{\mathbf{k}} = \epsilon - 2t\sum_\alpha \cos k_\alpha$. Here σ_α represent the Pauli matrices acting in the space of two independent orbitals per lattice site. For $\lambda, \lambda_z > 0$ and $2t < \epsilon < 6t$ the system described by Hamiltonian (3.31) is a TI in Z_2 class (1;000), i.e. a strong topological insulator. The magnetic field enters through the Peierls substitution, replacing all hopping amplitudes as $t_{ij} \to t_{ij} \exp\left[-(2\pi i/\Phi_0)\int_i^j \mathbf{A}\cdot d\mathbf{l}\right]$ and the Zeeman term $-g\mu_B\mathbf{B}\cdot\mathbf{s}/2$ where $\mu_B = e\hbar/2m_ec$ is the Bohr magneton. In the SC state the BdG Hamiltonian takes the form of Eq. (3.7) with $\Delta_{\mathbf{k}} = \Delta_0 i s_2$ describing on-site spin singlet pairing.

In the subsequent calculations we consider the above Hamiltonian on the real-space cubic lattice and in various wire geometries with rectangular cross sections and both periodic and open boundary conditions along the length of the wire. We find eigenstates and energy eigenvalues by the exact numerical diagonalization using standard LAPACK routines and by sparse matrix techniques in cases where only low-lying states are of interest. Unless explicitly stated otherwise we use the following set of model parameters in our subsequent calculations: $\lambda_z = 2\lambda$, $t = \lambda$, $\epsilon = 4\lambda$. This places our model into Z_2 class (1;000) and with $\lambda = 150$meV produces a bulk bandgap of 300meV, as in Bi_2Se_3 crystals.

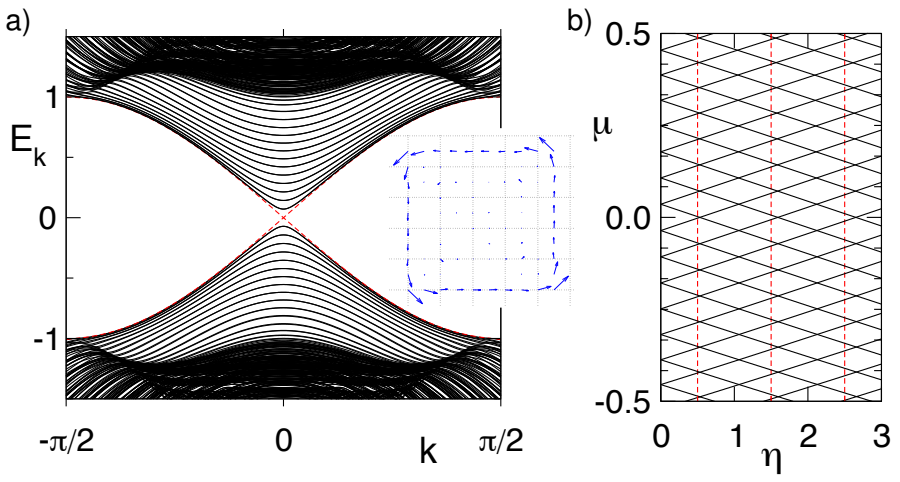

Figure 3.7: a) Energy dispersion for a long TI wire with 20×20 base described by lattice Hamiltonian (3.31) in the normal state with $\eta = 0.52$. For clarity only the low-energy portion of the spectrum is displayed in a part of the Brillouin zone. Inset shows the spin expectation values for the gapless state at small positive k. The length of the arrow is proportional to the wavefunction amplitude. b) Lines separating regions with different Majorana number $\mathcal{M} = -1(+1)$ extracted from the spectrum. All energies are in units of $\lambda = 150$meV and we use parameters $\lambda_z = 2$, $t = 1$, $\epsilon = 4$ and $g = 32$, corresponding to the strong TI phase with Z_2 index (1;000) and bulk bandgap $2\lambda = 300$meV.

Fig.3.7a shows a typical example of the excitation spectrum in an infinitely long wire with $W \times W$ cross-section in the normal state. We observe that for η close to $1/2$ the surface state is indeed gapless and the low-energy modes exhibit the expected pattern of degeneracy. Because of the surface state penetration into the TI bulk the surface electrons see a slightly smaller magnetic flux than the nominal flux $\Phi = BW^2$ given by the wire geometry and the gapless state is shifted to a slightly higher value of η. This is also seen in Fig. 3.7b which displays the Majorana number for the same system. This figure also indicates that for $\eta = 0.52(2n + 1)$ the system will be a 1D topological SC for any value of μ inside the bulk gap. Superconducting order opens a gap in the electron excitation spectrum as illustrated in Fig.3.8a. For an open-ended wire, crucially, our calculations reveal a pair of non-degenerate states at $\pm E_0$ inside the SC gap whose energies approach

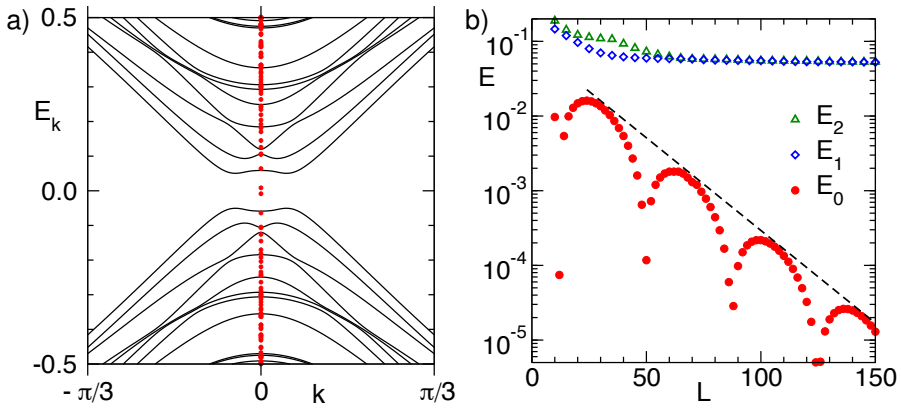

Figure 3.8: a) Energy bands for a long TI wire with 6×6 base in the SC state with $\eta = 0.49$, $\mu = 0.09$, $\Delta_0 = 0.08$ and $g = 0$ (solid lines), and the energy levels for $L = 36$ wire with open boundary conditions (red circles) obtained by exact numerical diagonalization. b) Three lowest positive energy eigenvalues obtained by the Lanczos method as a function of L. Dashed line represents the envelope function $0.089e^{-L/\xi}$ with $\xi = 17.5$.

zero for large L as $E_0 \propto e^{-L/\xi}$. Fig.3.8b illustrates this exponential decay (which is in addition modulated by oscillations at $2k_F$). Higher energy eigenstates approach non-zero values close to Δ_0 for large L. We have verified that the appropriate linear superpositions of the wavefunctions associated with the $\pm E_0$ eigenvalues are exponentially localized near the ends of the wire. The corresponding field operators then satisfy the Majorana condition $\hat{\psi}^\dagger = \hat{\psi}$, and represent, up to exponentially small corrections in their separation, the Majorana zero modes. As a last example of a calculation based on the lattice model we show in Fig. 3.9 the probablity density of Majorana end-states in a wire 100 lattice spacings long. We note that in any finite-length wire there will always be an exponentially small overlap between the two Majorana end-states. Such an overlap leads to the hybridization and a small non-zero energy δE for the combined fermionic state which shows probablity density equally split between the two ends of the wire. An (unphysical) state with equal probablity density exists at energy $-\delta E$. Fig. 3.9 shows how the Majorana end-states can be constructed by taking the appropriate linear superpositions of the above eigenstates. It is to be noted that for a finite-length wire the Majorana end-states are not true eigen-

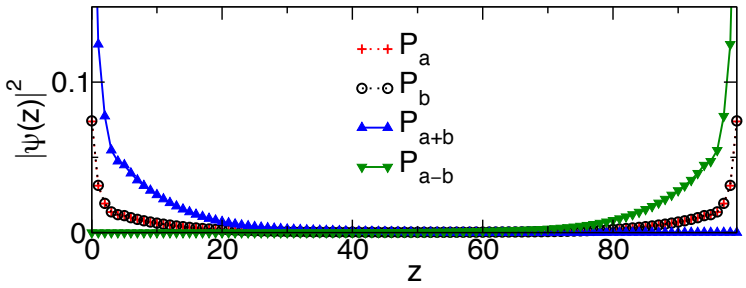

Figure 3.9: Probability densities of Majorana end-states. $P_{a/b}(z)$ represents the particle component of the wavefunction associated with $\pm E_0$ summed over x-y coordinates. $P_{a\pm b}$ represent the even/odd superpositions of these wavefunctions. The wire is 6 lattice sites wide in both the $\hat{x}$ and $\hat{y}$ directions and 100 lattice sites long in the $\hat{z}$ direction. $\eta = 0.49$ in units of the fundamental flux quantum, and the chemical potential $\mu = 0.09\lambda$, where $\lambda = 150$ meV.

states of the system; they will mix on a time scale $\hbar/\delta E$ which is, however, exponentially long in the wire length L.

3.3.2 The Majorana number and the topological phase diagram

The existence of MF at the ends of the wire depends on whether or not the wire is in the topological phase. For a 1D system the presence of the topological phase is indicated by Kitaev's Majorana number [81] $\mathcal{M}(H)$. In Fig.3.4, we show $\mathcal{M}(H)$ in different regions of the phase diagram in the limit $\Delta \to 0$ where it reflects simply the parity of the number of the Fermi points of the underlying normal state in the right half of the Brillouin zone. The resulting phase diagram in the η-μ plane, for μ inside the bulk bandgap, consists of diamond-shaped topological regions indicated in Fig. 3.10(a). In the limit $\Delta \to 0$ the individual diamonds just touch at their apices yielding a continuous topological phase for a specific value of magnetic flux η close to $\frac{1}{2}$ and for all values of μ inside the band gap. This feature underlies the key advantage of the present setup: the chemical potential does not require fine tuning. However, it is also true that when passing between individual diamond-shaped regions, the system gets arbitrarilly close to the phase boundary and one thus expect topological order to be rather fragile in

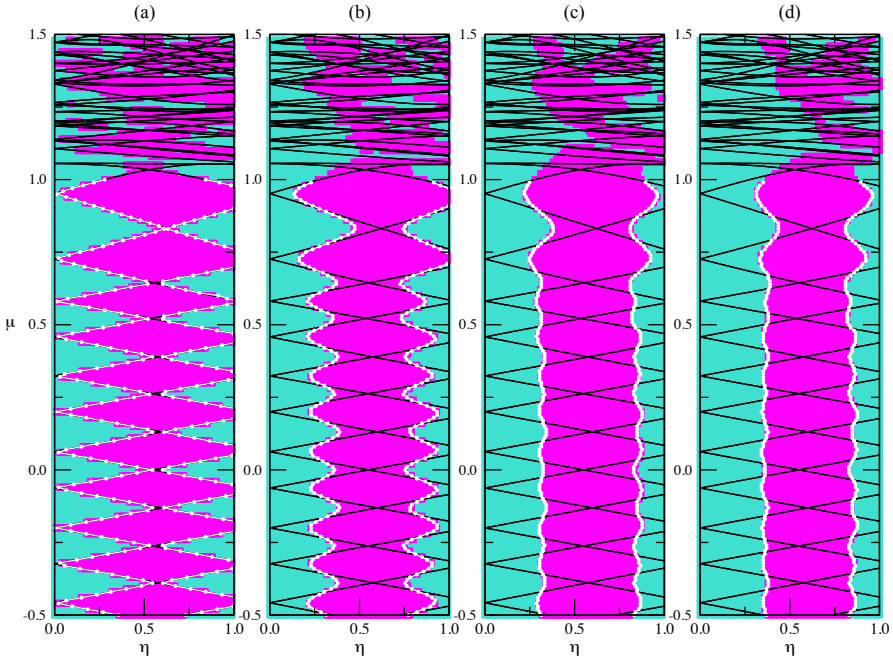

Figure 3.10: Phase diagrams computed from generalized Majorana number for the infinitely-long, clean wire with a 10 lattice site by 10 lattice site cross-section. (a), (b), and (c) are each for a system with a vortex, while the system with phase diagram (d) lacks a vortex. $|\Delta|$ is set to 0 and 0.04λ in (a), (b), respectively, and 0.08λ in both (c) and (d). Chemical potential μ is in units of $\lambda = 150$ meV and η is in units of the fundamental flux quantum. Blue and pink regions were created by computing the generalized Majorana number $\mathcal{M}$ in steps of at most $\Delta\eta = 0.02$ and $\Delta\mu = 0.02$, colouring these points blue ($\mathcal{M} = 1$, non-topological phase, no Majorana zero-modes in system) or pink ($\mathcal{M} = -1$, topological phase, Majorana zero-modes present in system), respectively, and enlarging these data points to create regions of solid colour. As well, the phase boundaries were computed (white lines) via a more efficient algorithm, with error bars at most the size of the symbols. White lines extend only up to $\mu = 1$ as at larger μ the topological phase regions break up into small domains and the algorithm used to compute the phase boundary is only effective for large, simply-connected regions of the phase diagram.

these regions. On the other hand, away from the $\Delta \to 0$ limit one intuitively expects the topological phase to become more robust and indeed this was suggested by the numerical results presented in Ref. [87]. In the following we shall elucidate this point and show that indeed for $\Delta_0 > 0$ the topological phase becomes a compact region in the η-μ plane.

We consider a general definition of the Majorana number[81]

$$\mathcal{M}(H) = \mathrm{sgn}\left[\mathrm{Pf}\tilde{B}(k=0)\right] \mathrm{sgn}\left[\mathrm{Pf}\tilde{B}(k=\frac{\pi}{a})\right], \tag{3.32}$$

where $\tilde{B}(k)$ is the position-space Hamiltonian of the infinite-length, lattice-model TI wire written in terms of Majorana fermion operators and Fourier-transformed in the $\hat{z}$-direction. a is the lattice-spacing, implying that $\tilde{B}(k)$ is evaluated here at $k = 0$ and at the edge of the Brillouin zone. Eq. (3.32) simplifies to the previously-given definition in [87] when $|\Delta|$ is sufficiently small.

We consider the phase diagram in two limiting situations: When Δ winds in phase counterclockwise by 2π around the circumference of the wire, corresponding to a vortex present along the length of the TI nanowire, and when Δ does not wind in phase, meaning there is no vortex in the system. These two situations are expected to represent the ground state of the system for the magnetic flux close to $\Phi_0/2$ and 0, respectively. The precise value of the flux at which the vortex enters will depend on details but we show below that, remarkably, the topological phase diagram is fairly insensitive to the presence or absence of the vortex.

Fig. 3.10 displays the phase diagram of a rectangular wire with a 10×10 cross section based on Eq. (3.32). As $|\Delta|$ is increased from zero, we see that the boundary of the region corresponding to the topological phase smoothes out, with the region centered close to $\eta = 0.5$ and extending through all values of the chemical potential inside the bulk band gap and also up into the bulk conduction band. We remark that the topological phase here is centered near a value of the magnetic flux that somewhat exceeds $\Phi_0/2$. This is because the surface state penetrates slightly into the bulk of the wire and thus encloses somewhat smaller amount of flux than the geometric surface area of the wire. For thicker wires this shift will be negligible.

It is also interesting to note that according to Fig. 3.10 the topological phase persists for μ well into the conduction band (as well as the valence band, which is not explicitly shown). This finding is potentially important in view of the fact that most TI crystals naturally grow with the chemical potential pinned inside the bulk conduction or valence band. We will show below, however, that although MFs indeed appear in this regime, the mini-

gap protecting them quickly collapses as μ moves deeper into the bulk band. Heuristically, one can understand this as follows. With μ inside the conduction band the bulk of the nanowire becomes metallic. In the presence of SC order and with the magnetic field applied along its axis there will be a vortex line running along its center. Such a vortex line will host low-energy core states with the characteristic energy scale Δ^2/E_F which quickly becomes very small as E_F increases (here E_F is the Fermi energy measured relative to the bottom of the bulk conduction band). By contrast when the chemical potential lies inside the bandgap the bulk of the wire remains insulating and does not contribute any low-energy states.

From study of the phase diagram Fig. 3.10 at $\Delta > 0$, we begin to understand the robustness of the Majorana bound states. Consider first the effect of non-magnetic disorder, modeled by introducing a spatially fluctuating component of the chemical potential $\mu \to \bar{\mu} + \delta\mu(\mathbf{r})$. Assume also that $\delta\mu(\mathbf{r})$ is slowly varying in space so that only variation along the z-direction are meaningful and $\mu(z)$ can be thought of as defining a phase of the wire in the vicinity of the coordinate z. If the average chemical potential $\bar{\mu}$ and the flux η are such that the system starts deep inside the topological phase then it is clear that fluctuations in $\delta\mu$ will not drive the system out of the topological phase unless they exceed the bulk bandgap. Similarly, fluctuations in the total magnetic flux η, which can occur e.g. in a wire with a non-uniform cross section, will not drive the system out of the topological phase unless they reach a significant fraction of $\Phi_0/2$. We demonstrate below by explicit inclusion of disorder in the lattice model that the heuristic argument given above remains valid even when disorder potential varies rapidly on the lattice scale.

The smoothing out of the topological region's boundary as $|\Delta|$ is increased can be understood by studying the low-energy analytical theory again. We start from the Hamiltonian in Eq. (3.8) and let $\mu = m = 0$, studying how the phase diagram changes for this value of the chemical potential as $|\Delta|$ is increased from zero. If we now assume that η deviates from $1/2$ by a small amount, i.e. $\eta = 1/2 + \delta\eta$ then the spectrum for the $l = 0$ branch can be written as

$$E_k = \pm \left[k^2 + \left(\frac{\delta\eta}{R} \pm \Delta_0 \right)^2 \right]^{1/2} . \tag{3.33}$$

We know that the system will be in the topological phase when $\delta\eta = 0$ and $\mu = 0^{\pm}$. To understand the smoothing out of the topological region's boundary, we identify when the spectral gap closes for non-zero Δ_0 as a

function of $\delta\eta$, since closing of the gap signifies a phase transition. We notice that the gap in Eq. (3.33) remains as $\delta\eta$ is moved away from 0 until $\delta\eta = \pm R\Delta_0/v\hbar$, where we have restored proper units. Therefore, we see that at $\mu = 0$, for nonzero Δ_0, the topological phase has widened from a point at $\eta = 1/2$ to an interval $(1/2 - R\Delta_0/v\hbar, 1/2 + R\Delta_0/v\hbar)$, as observed in the phase diagrams computed numerically using the more general definition of the Majorana number.

The absence or presence of a vortex in the TI nanowire makes negligible differences to the phase diagrams as seen by comparing Figs. 3.10(c) and 3.10(d). However, the presence or absence of a vortex does have a pronounced effect on the quasiparticle excitation gap Δ_{exc} (shown in Fig. 3.11) in the infinitely-long wire. From Fig. 3.11, we see that Δ_{exc} remains close in magnitude to $|\Delta|$ up until μ reaches the bottom of the bulk conduction band if the SC order parameter winds counter-clockwise in phase by 2π, while without a vortex Δ_{exc} can be seen to quickly decay with increasing μ. Clearly, near $\eta = 1/2$ the former represents a more physical situation.

If we study the minigap as a function of chemical potential with a vortex present, shown in Fig. 3.12, we see that, for μ close to zero, the minigap starts with an amplitude close to the SC gap Δ, in accord with the analytical theory presented in Sec. III.B. The minigap then continuously decreases with increasing μ, retaining a respectable value $\sim 0.1\Delta$ at the edge of the bulk conduction band at $\mu = 1$. As mentioned previously, the minigap then quickly collapses as the bulk bands are populated but nevertheless persists over a non-zero range of $\mu > 1$.

3.3.3 Robustness of Majorana fermions against disorder

As mentioned previously, we expect robustness of the Majorana end states with respect to non-magnetic disorder in the proposed device. There are two related but logically separate issues that pertain to this problem. First, we must ensure that SC order induced in the wire is itself robust against non-magnetic disorder. Since the device can be operated at (or very close to) the time-reversal invariant point and since we consider a spin-singlet s-wave SC order we expect this to be the case on the basis of Anderson's theorem. Below, we illustrate this aspect of the robustness by performing a self-consistent numerical calculation on our model in the presence of disorder. Second, we must show that Majorana end-states themselves remain stable in the presence of disorder. To some extent this already follows from our arguments in the previous subsection based on the study of the topological phase diagram. Also, stability of MFs follows from the stability of

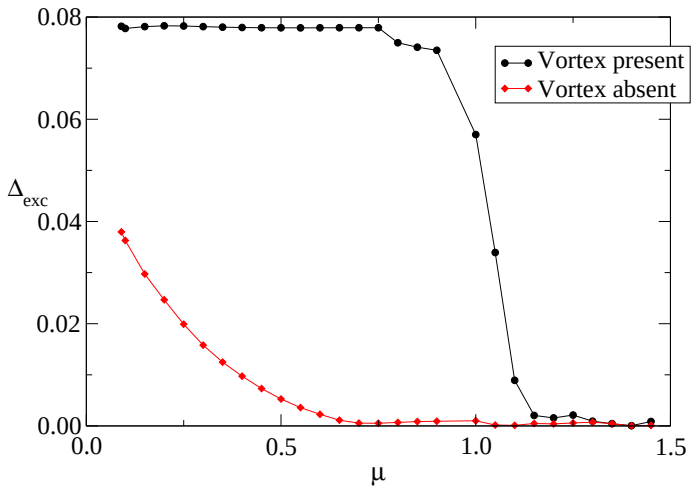

Figure 3.11: Quasiparticle excitation gap Δ_{exc} of an infinitely-long wire without disorder with a 14 lattice site by 14 lattice site cross-section as a function of chemical potential μ with vortex present (black circles) and vortex absent (red diamonds). Δ_{exc} and μ are expressed in units of $\lambda = 150$ meV. Here $|\Delta| = 0.08\lambda$.

the SC phase in the bulk of the wire argued above. Nevertheless, to address this question directly, we perform explicit numerical calculations for open-ended wires in the presence of non-magnetic disorder and in various physical regimes. These calculations confirm the expected robustness of MFs and yield additional insights into the quantitave aspects of this robustness; specifically they provide information about the minigap magnitude and the mechanism by which MFs are eventually destroyed in the strong-disorder limit.

To study these questions, we add a term corresponding to disorder in the on-site potential to the lattice Hamiltonian, H_0, of the clean system. The Hamiltonian for the system with disorder, H_{dis}, is therefore

$$H_{\text{dis}} = H_0 + \sum_{i\alpha} U_i c^\dagger_{i\alpha} c_{i\alpha'}, \tag{3.34}$$

where U_i, the random potential at lattice site i, is assigned a value from a uniform, random distribution ranging from $\frac{-U}{2}$ to $\frac{U}{2}$.

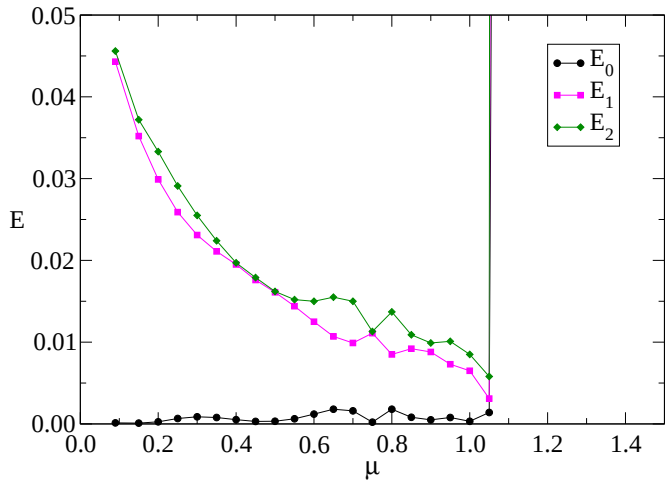

Figure 3.12: Three lowest energy eigenvalues E_2, E_1, and E_0 of the finite-length wire, without disorder, with 14 by 14 by 100 lattice sites as a function of chemical potential μ with vortex present with $|\Delta| = 0.08\lambda$. Δ_{exc} and μ are expressed in units of $\lambda = 150$ meV. Eigenvalues were computed via Lanczos method and failed to converge for $\mu > 1.05$, resulting in a non-physical spike to the non-convergent next data point.

As a first step we compute the magnitude of the SC order parameter self-consistently as described in [97] for different disorder strengths and with periodic boundary conditions along z, i.e. no Majorana end-states. This calculation assumes the existence of an intrinsic pairing potential V in the wire and is therefore, strictly speaking, not directly relevant to the proximity-induced SC state discussed in the rest of this paper. It nevertheless illustrates very nicely the robustness of the SC order with respect to disorder. The key point is that one would expect SC order to be even *more* robust when induced by proximity to the bulk superconductor. Fig. 3.13 shows mean SC order parameter magnitude vs. $\frac{U}{2}$ computed for different values of the pairing potential V. We observe that $|\Delta|_{\text{avg}}$ first decreases slightly with increasing U, but at larger U the mean SC order parameter increases in magnitude. We attribute this increase to the buildup of the normal density of states at the Fermi level, $N(\mu)$, due to disorder. Such a

buildup is known to occur in other 2D systems with a Dirac spectrum[98] and it should increase $|\Delta|$ according to the standard BCS formula[97]

$$\Delta = \hbar\omega_c e^{-1/N(\mu)V}. \tag{3.35}$$

Here ω_c and V are constants. These results suggest the SC order parameter is not only quite robust against non-magnetic disorder but the latter can actually enhance it when the chemical potential is close to the Dirac point.

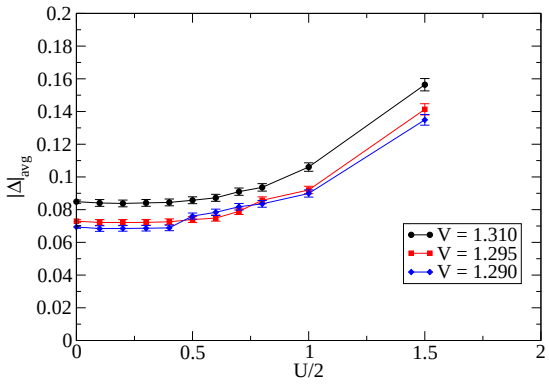

Figure 3.13: Mean superconducting order parameter magnitude $|\Delta|_{\text{avg}}$ for three different values of the pairing potential ($V = 1.310$, $V = 1.295$, and $V = 1.290$) as a function of disorder strength $\frac{U}{2}$. $|\Delta|_{\text{avg}}$ is averaged over every lattice site in a 6x6x6 lattice site nanowire with periodic boundary conditions in the $\hat{z}$-direction with random disorder in the chemical potential and also further averaged over 10 such randomly-disordered nanowires. The mean chemical potential for all data points is $\mu_{\text{avg}} = 0.09\lambda$. The self-consistent calculation for each disordered nanowire proceeded until the maximum difference in the superconducting order parameter magnitude between the final iteration and the next-to-last iteration of the calculation at any lattice site was less than 0.001λ.

To address the robustness of Majorana end-states we now study the finite-length wires. Using sparse matrix techniques, we solved for the average values of the three lowest, positive eigenvalues of the spectrum, and plotted these for a range of U, as shown in Fig. 3.14. These calculations are performed for a constant value of the SC gap, having previously established

that disorder has only a weak effect on the latter. We see that the energy of the Majorana bound state remains very close to zero, with no observable fluctuations. The topological SC is eventually destroyed by the collapse of the minigap, i.e. lowering of the excited states at some critical value of disorder strength U_c. It is interesting to note that U_c is rather large, being expressed in units of $\lambda = 150$ meV, exceeding the TI bulk bandgap by more than a factor of 5. Furthermore, the MFs are robust against disorder at a wide range of average chemical potential in the bulk band gap, although the minigap is largest for values close to the middle of the bulk band gap and smallest for values near the edge of the bulk band gap. We note that the minigap is roughly the same for mean chemical potential values of 0.09λ, 0.4λ, and 0.8λ if $\frac{U}{2} = \lambda$, suggesting disorder stabilizes the minigap in this regime. It is also interesting to note that for two larger values of μ disorder initially increases the minigap thus making the topological phase more robust.

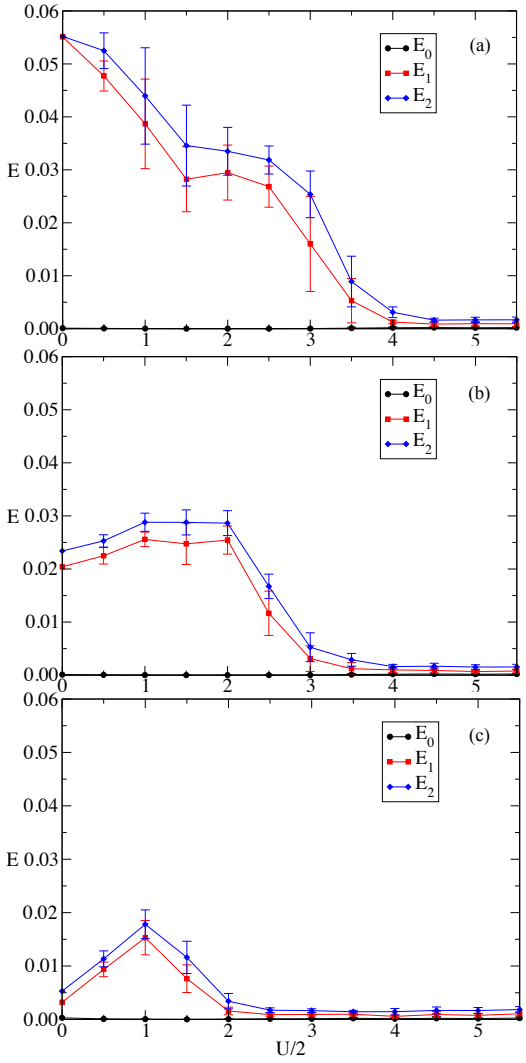

Figure 3.14: Three lowest positive energy eigenvalues E_0, E_1, and E_2 of a finite-length TI nanowire model with 6 by 6 by 100 lattice sites obtained by the Lanczos method as a function of disorder strength $\frac{U}{2}$ for mean chemical potential values of $\mu = 0.09$ (a), $\mu = 0.4$ (b), and $\mu = 0.8\lambda$. $|\Delta| = 0.08\lambda$ for each. $\frac{U}{2}$ and energy E are expressed in units of $\lambda = 150$ meV. The error bars reflect averaging over 10 independent realizations of the random potential.

3.4 Conclusion and discussion

The main goal of this work was to study the stability of Majorana zero-modes in the proposal introduced in [87], which consists of a TI nanowire, proximity-coupled to a bulk s-wave superconductor, with a weak magnetic field applied along the nanowire's length. After reviewing the literature to illustrate the importance of identifying a device in which MFs emerge under a wide range of accessible conditions, and reviewing the theory behind the proposed device in greater detail than possible in [87], we studied the robustness of the topological superconductor phase of the device against disorder.

As a first step we computed the topological phase diagram of the TI nanowire numerically in a semi-realistic lattice model. Using a general definition of Kitaev's Majorana number[81] $\mathcal{M}(H)$ we were able to show that for non-zero values of SC order parameter Δ the topological phase forms a set of compact columnar regions in the plane spanned by the magnetic flux $\eta = \Phi/\Phi_0$ and the chemical potential μ, centered around half-integer values of ν and covering about 50% of the phase diagram (see Fig. 3.10). This form of the phase diagram confers two principal advantages of our proposed device as regards future experimental realizations and potential applications: (i) unlike in the semiconductor wire realizations[13] where significant fine-tuning of the chemical potential is required to reach the topological phase, our proposed device produces Majorana end-states for μ anywhere inside the bulk bandgap of the TI; and (ii) if the average chemical potential of the nanowire is in the bulk band gap, we can expect the entire nanowire to remain in the topological phase even for large disorder strengths, as even then any local chemical potential value will remain in the topological region of the phase diagram. We also observe from the phase diagram Fig. 3.10 that the topological phase persists over a wide range in magnetic flux through the cross-section of the nanowire. This feature is less critical because the magnetic field can be easily tuned in a laboratory. Nevertheless understanding the magnetic phase boundary is very useful since changing the magnetic field strength can be used to tune the wire between topological and normal phases.

To explicitly ascertain the robustness of the MF with respect to thermal fluctuations and non-magnetic disorder we studied the system's minigap by both analytic and numerical techniques. Minigap, defined as the smallest non-zero energy level in the system, can be taken as a good proxy for the robustness of the quantum information encoded in MFs since uncontrolled excitations of quasiparticles out of the ground state into the low-lying ex-

cited states would obviously spoil such encoding. Also, large values of the minigap can aid experimental detection of the Majorana zero mode using various spectroscopic techniques. We use the low-energy, analytical theory of [87] to first show that excited states should be close in energy to the magnitude of the superconducting gap when the chemical potential is close to the middle of the bulk band gap of the TI nanowire, indicating Majorana zero-modes in the device should be protected by a sizeable minigap. We then employ the lattice model and compute the three lowest eigenenergies of the TI nanowire with disorder to show that the minigap remains significant even for the disorder strength considerably exceeding the bulk band gap of the TI. Interestingly, we find that disorder strength comparable to the magnitude of the bulk bandgap also appears to stabilize the minigap at a sizeable value over changes in the average chemical potential in the nanowire, which might be useful in future applications of the device.

Here we make some comments on the experimental realization. For the existing Bi_2Se_3 nanoribbons [84, 85] with cross-sectional area $S \approx 6 \times 10^{-15}\text{m}^2$ the surface level spacing is $\delta E_S \simeq v\hbar\sqrt{\pi/S} \simeq 7\text{meV}$. At half flux quantum, which corresponds to the magnetic field strength $B = \Phi_0/2S \simeq 0.34\text{T}$, the Zeemann energy scale $\delta E_Z = g\pi\hbar^2/2m_eS \simeq 0.6\text{meV}$ (taking $v = 5 \times 10^5\text{m/s}$ and $g = 32$) and thus probably negligible. On the other hand experiments on planar Sn-Bi_2Se_3 interfaces [88] show induced SC gap $\sim 0.2\text{meV}$, a significant fraction of the native Sn bulk gap ($\sim 0.6\text{meV}$). It thus appears conceivable that a pairing gap of several meV could be induced in Bi_2Se_3 nanoribbons by using in place of Sn a superconductor with larger bulk gap, such as NbTiN or MgB_2. In such devices it should then be possible to employ scanning tunneling techniques to detect the zero modes in addition to previously discussed transport measurements [20, 39, 81]. Another intriguing possibility is to fabricate nanoribbons from $Cu_xBi_2Se_3$ which becomes a superconductor below 4K [89] while simultaneously retaining the protected surface states in [90].

Before concluding we address the following question: Do MFs predicted to exist in our device obey non-Abelian exchange statistics? This property is obviously of paramount importance for any future application in quantum information processing. Alicea et al. [91] clarified the sense in which MFs in 1D wire networks exhibit non-Abelian statistics upon exchange, considering semiconductor wires[13, 20, 39], and showed how particle exchanges can be effected in such a setting. Although superficially similar to these models[20, 39] our proposal is more closely related to the original Fu-Kane vortex at the interface between a TI and an ordinary superconductor[37]. Indeed consider a thought experiment in which we take our wire and slowly increase its radius

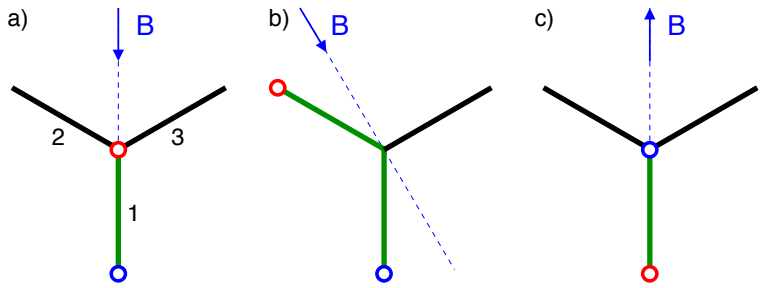

Figure 3.15: Exchange of MFs in a trijunction device. a) The field **B** is tuned so that nanowire 1 has flux close to $\Phi_0/2$ through its cross section and is thus in the topological phase with MFs localized near its ends. The flux through wires 2 and 3 is down by the factor $\cos(2\pi/6) = 0.5$ and they are thus in the trivial phase. b) Rotating the direction of **B** by 30° the flux through wires 1 and 2 becomes $\cos(2\pi/12)(\Phi_0/2) \simeq 0.866(\Phi_0/2)$ and is thus sufficiently close to $\Phi_0/2$ for them both to be in the topological phase according to the phase diagram in Fig. 3.10. As a result the MF previously located at the junction (red circle) has now moved to the other end of wire 2 as indicated. Continuing this process by rotating **B** further in 30° increments it is easy to map out the motion of MFs and conclude that after 180° rotation the system comes back to the original situation with MFs localized on wire 1 but with their order exchanged as illustrated in panel c).

while simultaneously reducing the applied magnetic field so that the total flux through its cross section remains constant at $\Phi_0/2$. We also assume that all the surfaces of the resulting disk remain covered by a thin SC film. In the limit when the radius R becomes comparable to the wire length L we have a bulk disk-shaped TI covered with a SC film. The presence of $\Phi_0/2$ flux and the cylindrical symmetry dictates that a vortex must be present at the center of each of the flat disk surfaces. Such vortices will contain MFs[37] and will obey non-Abelian exchange statistics according to the standard arguments. MFs in our wires are thus adiabatically connected to those residing in the cores of Fu-Kane vortices and are thus expected to obey the same non-Abelian exchange statistics when organized into T-junctions or wire network geometries[91]. In Fig. 3.15 we outline a simple protocol that implements an exchange of two MFs in a symmetric 'trijunction' device formed by three nanowires joined at a single point. The exchange of two MFs, initially localized at the ends of one of the wires, is effected simply by a 180° rotation of the applied magnetic field in the plane of the device.

We conclude that unpaired Majorana zero-modes are exceptionally stable in our proposed device, being present over a wide range in magnetic flux, chemical potential, and disorder strength, with disorder even being expected to stabilize the MFs to an extent. They obey non-Abelian exchange statistics by virtue of being adiabatically connected to the Fu-Kane vortex[37] and, as illustrated above, can be easily manipulated by changing the direction of the applied magnetic field. On this basis we expect the device architecture discussed in this work to be useful for future experimental study of MFs and their potential applications.

Bibliography

[1] T. D. Ladd *et al.*, Nature **464**, 45-53 (2010).

[2] P. W. Shor, Phys. Rev. A **52**, R2493 (1995).

[3] J. Alicea *et al.*, Nature Physics **7**, 412-417 (2011).

[4] C. Nayak, S. H. Simon, A. Stern, M. Freedman, and S. Das Sarma, Rev. Mod. Phys., 5**80**, 1083 (2008).

[5] A. Kitaev, Ann. Phys. **303**, 2 (2003).

[6] E. Majorana, Nuovo Cimento **5**, 171 (1937).

[7] C. W. J. Beenakker, arXiv:1112.1950v2 (unpublished).

[8] M. H. Freedman, Proc. Natl. Acad. Sci., **95**, 98 (1998).

[9] M. H. Freedman, A. Kitaev, M. J. Larsen, and Z. Wang, Bull. Amer. Math. Soc., **40**, 31 (2003).

[10] S. Das Sarma, M. Freedman, and C. Nayak, Phys. Rev. Lett., **94**, 166802 (2005).

[11] P. Bonderson, M. Freedman, and C. Nayak, Phys. Rev. Lett., **94**, 166802 (2005).

[12] J. R. Williams, A. B. Beswick, P. Gallagher, S. S. Hong, Y. Cui, A. S. Bleich, J. G. Analytis, I. R. Fisher, and D. Goldhaber-Gordon, arXiv:1202.2323.

[13] V. Mourik, K. Zuo, S. M. Frolov, S. R. Plissard, E. P. A. M. Bakkers, and L. P. Kouwenhoven, Signatures of Majorana fermions in hybrid superconductor- semiconductor nanowire devices, Science (April 12, 2012).

[14] L.P. Rokhinson, X. Liu and J. Furdyna, arXiv:1204.4212

[15] J. Alicea, arXiv:1202.1293v1 (unpublished).

[16] C. Nayak *et al.*, Rev. Mod. Phys. **80**, 1083 (2008).

[17] P. W. Shor, Phys. Rev. A 52, R2493 (1995).

[18] G. Moore and N. Read, Nucl. Phys. B 360, 362 (1991).

[19] G. E. Volovik, The Universe in a Helium Droplet (Oxford University Press, 2003).

[20] Y. Oreg, G. Refael and F. von Oppen, Phys. Rev. Lett. **105**, 177002 (2010).

[21] A. C. Potter and P. A. Lee, Phys. Rev. B, **83**, 184520 (2011).

[22] P. Anderson, Journal of Physics and Chemistry of Solids, **11**, 26 (1959).

[23] J. D. Sau, R. M. Lutchyn, S. Teari, and S. Das Sarma, Phys. Rev. B, **82**, 094522 (2010).

[24] C. L. Kane and E. J. Mele, Phys. Rev. Lett., **95**, 226801 (2005).

[25] D. Xiao, W. Zhu, Y. Ran, N. Nagaosa, and So. Okamoto, Nat. Comm. **2**, 596 (2011).

[26] S. Murakami, Phys. Rev. Lett., **97**, 236805 (2006).

[27] B. A. Bernevig, T. L. Hughes, and S.-C. Zhang, Science, **314**, 1757 (2006).

[28] C. Liu, T. L. Hughes, X.-L. Qi, K. Wang, and S.-C. Zhang, Phys. Rev. Lett., **100**, 236601 (2008).

[29] C.-C. Liu, W. Feng, and Y. Yao, Phys. Rev. Lett., **107**, 076802 (2011).

[30] C. Weeks, J. Hu, J. Alicea, M. Franz, and R. Wu, Phys. Rev. X, **83**, 184520 (2011).

[31] M. Konig, S. Wiedmann, C. Brune, A. Roth, H. Buhmann, L. W. Molenkamp, X.-L. Qi, and S.-C. Zhang, Science, **325**, 766 (2007).

[32] A. Roth, C. Brune, H. Buhmann, L. W. Molenkamp, J. Maciejko, X.-L. Qi, and S.-C. Zhang, Science, **325**, 294 (2009).

[33] I. Knez, R.-R. Du, and G. Sullivan, Phys. Rev. Lett., **107**, 136603 (2011).

[34] I. Knez, R.-R. Du, and G. Sullivan, arXiv:1006.5819 (unpublished).

[35] J. B. Miller, D. M. Zumbühl, C. M. Marcus, Y. B. Lyanda-Geller, D. Goldhaber-Gordon, K. Campman, and A. C. Gossard, Phys. Rev. Lett., **90**, 076807 (2003).

[36] L. Meier, G. Salis, I. Shorubalko, E. Gini, S. Schön, and K. Ensslin, Nature Physics, **3**, 650 (2007).

[37] L. Fu and C. L. Kane, Phys. Rev. Lett., **100**, 096407 (2008).

[38] B. Seradjeh and E. Grosfeld, Phys. Rev. B, **83**, 174521 (2011).

[39] R.M. Lutchyn, J.D. Sau and S. Das Sarma, Phys. Rev. Lett. **105**, 077001 (2010).

[40] J. D. Sau, S. Tewari, and S. Das Sarma, Phys. Rev. B **85**, 064512 (2012).

[41] K. Flensberg, Phys. Rev. B, **82**, 180516 (2010).

[42] A. R. Akhmerov, J. P. Dahlhaus, F. Hassler, M. Wimmer, and C. W. J. Beenakker, Phys. Rev. Lett., **106**, 1057001 (2011).

[43] I. C. Fulga, F. Hassler, A. R. Akhmerov, and C. W. J. Beenakker, Phys. Rev. B, **83**, 155429 (2011).

[44] P. W. Brouwer, M. Duckheim, A. Romito, and F. von Oppen, Phys. Rev. B, **144526**, 144526 (2011).

[45] P. W. Brouwer, M. Duckheim, A. Romito, and F. von Oppen, Phys. Rev. Lett., **107**, 196804 (2011).

[46] T. D. Stanescu, R. M. Lutchyn, and S. Das Sarma, Phys. Rev. B, **84**, 144522 (2011).

[47] C. Bena, D. Sticlet, and P. Simon, Phys. Rev. Lett. **108**, 096802 (2012).

[48] S. Nadj-Perge, V. S. Pribiag, J. W. G. van den Berg, K. Zuo, S. R. Plissard, E. P. A. M. Bakkers, S. M. Frolov, and L. P. Kouwenhoven, Phys. Rev. Lett. **108**, 166801 (2012).

[49] S. Gangadharaiah, B. Braunecker, P. Simon, and D. Loss, Phys. Rev. Lett., **107**, 036801 (2011).

[50] B. Braunecker, P. Simon, and D. Loss, Phys. Rev. B, **80**, 165119 (2009).

[51] E. M. Stoudenmire, J. Alicea, O. A. Starykh, and M. P. Fisher, Phys. Rev. B., **84**, 014503 (2011).

[52] A. Romito, J. Alicea, G. Refael, and F. von Oppen, arXiv:1110.6193 (2011).

[53] M. Wimmer, A. R. Akhmerov, M. V. Medvedyeva, J. Tworzydło, and C. W. J. Beenakker, Phys. Rev. Lett., **105**, 046803 (2010).

[54] M. Gibertini, F. Taddei, M. Polini, and R. FazioPhys. Rev. B **85**, 060507(R) (2012).

[55] J. D. Sau, C. H. Lin, H.-Y. Hui, and S. Das Sarma, Phys. Rev. Lett. **108**, 067001 (2012).

[56] W. DeGottardi, D. Sen, and S. Vishveshwara, New Yournal of Physics, **13**, 065028 (2011).

[57] J. D. Sau and S. Das Sarma, arXiv:1111.6600 (unpublished).

[58] J. Klinovaja, M. J. Schmidt, B. Braunecker, and D. Loss, Phys. Rev. B, **84**, 085452 (2011).

[59] J. D. Sau and S. Tewari, arXiv:1111.5622 (unpublished).

[60] J. Klinovaja, S. Gangadharaiah, and D. Loss, arXiv:1201.0159 (unpublished).

[61] L. P. Gor'kov and E. I. Rashba, Phys. Rev. Lett., **87**, 037004 (2001).

[62] M. Duckheim and P. W. Brouwer, Phys. Rev. B, **83**, 054513 (2011).

[63] A. Yu. Kasumov, O. V. Kononenko, V. N. Matveev, T. B. Borsenko, V. A. Tulin, E. E. Vdovin, and I. I. Khodos, Phys. Rev. B **77**, 3029 (1996).

[64] D. Zhang, J. Wang, A. M. DaSilva, J. S. Lee, H. R. Gutierrez, M. H. W. Chan, J. Jain, and N. Samarth, Phys. Rev. B **84**, 165120 (2011).

[65] J. Wang, C.-Z. Chang, H. Li, K. He, D. Zhang, M. Singh, X.-C. Ma, N. Samarth, M. Xie, Q.-K. Xue, and M. H. W. Chan, Phys. Rev. B **85**, 045415 (2012).

[66] B. Sacepe, J. B. Oostinga, J. L. Li, A. Ubaldini, N. J. G. Couto, E. Giannini, and A. F. Morpurgo, Nat. Comm. 2, 575 (2011).

[67] M. Veldhorst, C. G. Molenaar, X. L. Wang, H. Hilgenkamp, and A. Brinkman, Appl. Phys. Lett. 100, 072602 (2012).

[68] F. Qu, F. Yang, J. Shen, Y. Ding, J. Chen, Z. Ji, G. Liu, J. Fan, X. Jing, C. Yang, and L. Lu, arXiv:1112.1683.

[69] S. Sasaki, M. Kriener, K. Segawa, K. Yada, Y. Tanaka, M. Sato, and Y. Ando, Phys. Rev. Lett. **107**, 217001 (2011).

[70] G. Koren, T. Kirzhner, E. Lahoud, K. B. Chashka, and A. Kanigel, Phys. Rev. B **84**, 224521 (2011).

[71] F. Yang, Y. Ding, F. Qu, J. Shen, J. Chen, Z. Wei, Z. Ji, G. Liu, J. Fan, C. Yang, T. Xiang, and L. Lu, Phys. Rev. B **85**, 104508 (2012).

[72] M.-X. Wang, C. Liu, J.-P. Xu, F. Yang, L. Miao, M.-Y. Yao, C. L. Gao, C. Shen, X. Ma, X. Chen, Z.-A. Xu, Y. Liu, S.-C. Zhang, D. Qian, J.-F. Jia, and Q.-K. Xue, Science 336, 5255 (2012).

[73] Hasan, M.Z.; Kane, C.L. Rev. Mod. Phys. **82** (4): 3045 (2010).

[74] Schnyder, A. P., S. Ryu, A. Furusaki, and A. W. W. Ludwig, Phys. Rev. B **78**, 195125 (2008).

[75] Kitaev, A., AIF Conf. Proc. **1134** 22 (2009).

[76] Schnyder, A. P., S. Ryu, A. Furusaki, and A. W. W. Ludwig, AIP Conf. Proc. **1134**, 10 (2009).

[77] Ryu, S., A. Schnyder, A. Furusaki, and A. W. W. Ludwig, New J. Phys. **12**, 065010 (2010).

[78] Fu, L., C. L. Kane, and E. J. Mele, Phys. Rev. Lett. **98** 106803 (2007).

[79] Moore, J. E., and L. Balents, Phys. Rev. B **75**, 121306(R) (2007).

[80] Roy, R., Phys. Rev. B **79**, 195322 (2009).

[81] A.Y. Kitaev, Phys. Usp. **44**, 131 (2001).

[82] Halperin, B. I., Phys. Rev. B **25**, 2185 (1982).

[83] D. Kong, *et al.*, Nano Lett. **10**, 329 (2010).

[84] H. L. Peng, *et al.*, Nature Mat. **9**, 225 (2010).

[85] H. Tang, *et al.*, ACS Nano **5**, 7510 (2011).

[86] D. Zhang, *et al.*, Phys. Rev. B **84**, 165120 (2011)

[87] A. Cook and M. Franz, Phys. Rev. B **84**, 201105(R) (2011).

[88] F. Yang. *et al.*, Phys. Rev. B **85**, 104508 (2012).

[89] Y.S. Hor *et al.*, Phys. Rev. Lett. **104**, 057001 (2010).

[90] L.A. Wray *et al.*, Nature Phys. **6**, 855 (2010).

[91] J. Alicea, Y. Oreg, G. Refael, F. von Oppen, M.P.A. Fisher, Nature Phys. **7**, 412 (2011).

[92] P. M. Ostrovsky, I. V. Gornyi, A. D. Mirlin, Phys. Rev. Lett. **105**, 036803 (2010).

[93] R. Jackiw and P. Rossi, Nucl. Phys B **190**, 681 (1981).

[94] X.-L. Qi, S.-C. Zhang, arXiv:1008.2026

[95] S. Tewari, T. D. Stanescu, J. D. Sau, S. Das Sarma, arXiv:1204.3637v2 (unpublished).

[96] L. Fu and E. Berg, Phys. Rev. Lett. **105** 097001, (2010).

[97] M. Tinkham, *Introduction to Superconductivity* (McGraw Hill, New York) 1996.

[98] N.M.R. Peres, F. Guinea, and A.H. Castro Neto, Phys. Rev. B **73**, 125411 (2006).